# Intraseasonal variability in South America recorded in stable water isotopes

Christophe Sturm, Françoise Vimeux, Gerhard Krinner

# Intraseasonal variability in South America recorded in stable water isotopes

Christophe Sturm,[1,2,4] Françoise Vimeux,[3] and Gerhard Krinner[1]

Received 30 November 2006; revised 27 June 2007; accepted 14 August 2007; published 30 October 2007.

[1] The recent number isotopic records extracted from Andean ice cores (South America) has illustrated the key role such archives can play in past climate reconstructions. Nevertheless, interpreting isotopic archives as quantified climate proxies requires an understanding of which climate parameters control the stable isotopic composition of water. Mesoscale modeling sheds new light on the meteorological mechanisms dominant during austral summer. Here we focus on the variability of the South Atlantic Convergence Zone (SACZ) and its repercussions on upstream regions. The SACZ is a major component of the South American Monsoon System (SAMS). The present study uses the isotopic signature of the SAMS, as simulated by the stable water isotope enabled regional circulation model REMO$_{iso}$ to answer the question: how does the SAMS affect the isotopic composition of precipitation during the wet season? In order to analyze the internal, purely atmospheric variability mode, the model was forced by climatological sea-surface temperatures. We investigate the concurrent intraseasonal variability of meteorological and isotopic parameters at pentad (5 days) interval using empirical orthogonal functions (EOFs). REMO$_{iso}$ reproduces the main meteorological characteristics of the SAMS consistent with observations as well as previous modeling studies. Furthermore, we demonstrate that $\delta^{18}$O integrates both circulation and precipitation variability. This new evidence contributes to the comprehension of the $\delta^{18}$O signal in tropical South America, highlighting the internal atmospheric variability, as opposed to external forcing by Pacific and Atlantic sea-surface temperature.

**Citation:** Sturm, C., F. Vimeux, and G. Krinner (2007), Intraseasonal variability in South America recorded in stable water isotopes, *J. Geophys. Res.*, *112*, D20118, doi:10.1029/2006JD008298.

## 1. Introduction

[2] Recent studies have underlined the sensitivity of the Tropics to global climate fluctuations [*Chiang and Sobel*, 2002; *Thompson et al.*, 1995; *Thompson*, 2000]. Isotopic records from tropical high altitude ice cores and low-land speleothems hence provide a unique archive of past climate variability. Most of the tropical glaciers worldwide are located in The Andean Cordillera, with summits exceeding 6000 m. Several ice cores were recovered from the Andes, with climate archives extending back to 25 ka [*Thompson et al.*, 1998, 2000; *Ramirez et al.*, 2003] as well as providing seasonal precipitation records for the last centuries. In addition to the ice core records available for the region low elevation calcite speleothems are also available from north-east [*Wang et al.*, 2004] and south-east Brazil [*Cruz et al.*, 2006]. The isotopic signal is here expressed as the depletion of the heavy isotope $H_2^{18}O$ relative to the Vienna standard mean ocean water (V-SMOW), by the following equation:

$$\delta^{18}O = \left( \frac{[H_2^{18}O]/[H_2O]_{sample}}{[H_2^{18}O]/[H_2O]_{SMOW}} - 1 \right) \cdot 1000\ [‰]. \qquad (1)$$

[3] The physical processes controlling the isotopic composition of South American precipitation are still under investigation. Statistical evidence shows that the interannual variability is controlled by sea-surface temperatures in the Tropical Pacific [*Bradley et al.*, 2003; *Thompson et al.*, 2000], although moisture originates from the Atlantic. *Hoffmann* [2003], *Hoffmann et al.* [2003], and *Henderson et al.* [1999] report that the isotopic signal in ice cores primarily records changes in precipitation and circulation patterns over the Amazon and the equatorial Atlantic. *Pierrehumbert* [1999] investigated possible controls on $\delta^{18}$O using Rayleigh-type distillation models, but failed to represent the varying trajectories of air masses precipitating over the Andes. *Vimeux et al.* [2005] examine the climatic controls on the modern isotopic composition of precipitation in the Zongo Valley (Bolivia), upstream of the Illimani ice core drilling site.

[1] Laboratoire de Glaciologie et Géophysique de l'Environnement, Saint-Martin-d'Hères Cedex, France.
[2] Max-Planck Institute for Meteorology, Hamburg, Germany.
[3] IRD-UR Great Ice, IPSL/LSCE (Laboratoire des Sciences du Climat et de l'Environnement), Gif-sur-Yvette, France.
[4] Currently at Bjerknes Centre for Climate Research, NO-Bergen.


0148-0227/07/2006JD008298

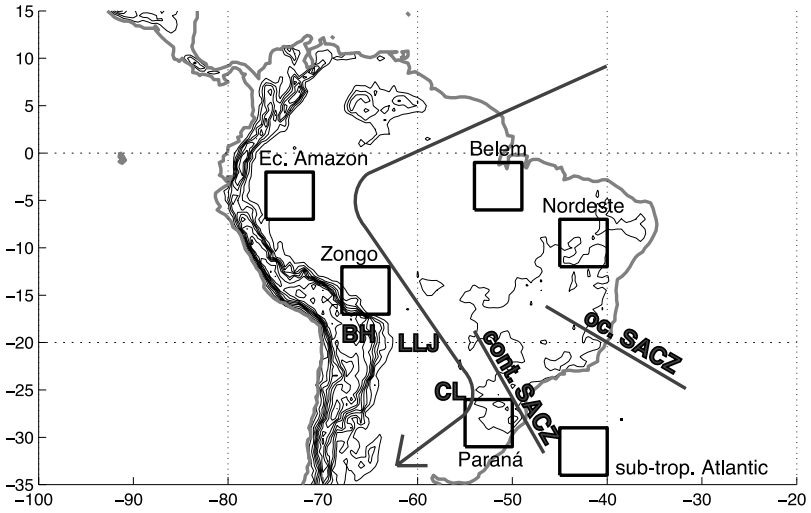


**Figure 1.** Topography of the study domain at 0.5 resolution. Contours represent 500 m altitude isolines. The 5° × 5° black boxes show the location and respective name of the sites listed in Table 2. Bold acronyms represent the major features of the South American Monsoon System (SAMS), after *Zhou and Lau* [1998]. BH: Bolivian High, CL: Chaco low, LLJ: low-level jets, SACZ: South Atlantic Convergence Zone. The continental and oceanic locations of the SACZ are indicated by gray lines. The bended arrow represents low-level cross-equatorial flow.

[4] *Vuille et al.* [2003b, 2003a] conducted a comprehensive study of climate controls on $\delta^{18}$O within isotope enabled GISS-II and ECHAM4 general circulation models. The authors conclude that the El Niño southern oscillation (ENSO) and associated sea surface temperature (SST) anomalies coincide best with inter-annual variability of $\delta^{18}$O over South America, in particular in tropical ice cores.

[5] However, recent observational and modeling studies have also identified physical mechanisms that control circulation and precipitation at intraseasonal timescales [*Grimm et al.*, 2004; *Nogues-Paegle et al.*, 2003]. These meteorological mechanisms are all components of the South American monsoon system (SAMS) summarized in Figure 1. The SAMS reaches its mature stage during summer (DJF), and accounts for up to 80% of annual rainfall in tropical and sub-tropical areas. Like the east Asian monsoon, typical monsoon features develop across South America, as depicted by *Zhou and Lau* [1998]. Low-level cross equatorial flow advects moist, warm air that is deviated polewards. Sub-tropical low-level highs over the ocean contrasts with a thermal low over the continent (Chaco low). At upper levels, an anti-cyclonic circulation develops above the continent (Bolivian high). An intense convergence zone develops over the south-east coast of Brazil (south Atlantic convergence zone - SACZ), which explains the heavy summertime precipitation. Some dominant features of the SAMS, especially north-westerly low-level jets (LLJ) are mesoscale features. Being influenced by local (topography) effects, the LLJ are better represented in regional models than in coarser GCM or re-analyses [*Vernekar et al.*, 2003; *Chou et al.*, 2000; *Rocha and Ambrizzi*, 2004; *Rojas and Seth*, 2003; *Seth and Rojas*, 2003; *Seth et al.*, 2004].

[6] Given the importance of features such as the LLJ evidence from meso-scale modeling over South America should greatly refine the understanding of isotope-climate relations in the region already gained from coarses global circulation models. To what extend does the mesoscale SAMS influence the $\delta^{18}$O signal over tropical and sub-tropical South America? *Vuille and Werner* [2005] explored the isotopic signature of the SAMS. Focusing on inter-annual variability and the impact of Pacific SST patterns (typically El Niño versus La Niña situations). In addition to being limited by the coarse resolution and simplified topography of a GCM, this study did not examine the intraseasonal variability, which is typical of the SAMS mechanism.

[7] The present study focuses on intraseasonal (DJF) variability of the SACZ/SAMS using the regional circulation model REMO$_{iso}$, fitted with stable water isotope diagnostics. To identify the singular modes of atmospheric variability, we cancel any oceanic forcing by applying climatological SST as boundary conditions to REMO$_{iso}$. This cancels inter-annual variability primarily related to ENSO, but also to any Atlantic SST anomalies. *Sturm et al.* [2007] compared REMO$_{iso}$ to coarser ECHAM4 GCM simulations, as well as gridded precipitation and station $\delta^{18}$O observations. REMO$_{iso}$ accurately reproduces the mean annual cycle of precipitation (albeit a general overestimation of precipitation), circulation and $\delta^{18}$O over South America.

[8] In the second section, we introduce the regional circulation model REMO$_{iso}$ and its stable water isotope module. On the basis of empirical orthogonal function (EOF) analysis, we describe the dominant mode of intraseasonal variability, which is shared by various climate parameters. The third section demonstrates that the bimodal distribution of precipitation simulated by REMO$_{iso}$ is related to location of the SACZ. Other typical features of the SAMS in low- and upper-level atmospheric circulation

are well reproduced by REMO$_{iso}$. The fourth section concentrates on the $\delta^{18}$O signal, which records distinctively the SAMS variability introducing a novel way of using $\delta^{18}$O as a proxy for SAMS variability. In the last section, we discuss previous results in order to assess the meteorological processes controlling the $\delta^{18}$O signal in South America, and its implications for the interpretation of isotopic climate archives.

## 2. Model and Methods

### 2.1. REMO Experiment With Climatological SST

[9] The regional circulation model REMO was originally developed for weather prognosis by the German Weather Service (DWD - Deutscher Wetterdienst [*Majewski*, 1991]). It was later adapted to climate purposes at the Max-Planck-Institute for Meteorology [*Jacob et al.*, 2001] by incorporating the physics scheme of the ECHAM general circulation model [*Roeckner et al.*, 1996]. Similarly, a stable water isotope module developed for ECHAM [*Hoffmann et al.*, 1998; *Werner and Heimann*, 2002] was adapted to REMO. A detailed description of REMO and its stable water isotope module is given by *Sturm et al.* [2005].

[10] REMO runs at a 0.5°, i.e., ~55 km horizontal resolution and 19 vertical hybrid $\sigma$-pressure levels. The study domain spans the tropical South American continent and surrounding oceans, from 100°W to 20°W in longitude and 35°S to 15°N in latitude (Figure 1). The specific features of the physics scheme are described by *Roeckner et al.* [1996].

[11] REMO computes the stable water isotope fractionation processes using the same module as ECHAM [*Hoffmann et al.*, 1998]. The isotopic module computes equilibrium [*Majoube*, 1971] and kinetic [*Merlivat and Jouzel*, 1979; *Jouzel and Merlivat*, 1984] fractionation for *HDO* and $H_2^{18}O$ at each model time step. The cloud microphysics computes fractionation processes between solid, liquid and gaseous phases of water, including the different diffusion constants in ice at low temperatures for *HDO* and $H_2^{18}O$ [*Jouzel and Merlivat*, 1984]. To account for sub-cloud evaporation of raindrops, their isotopic composition is set in partial equilibrium with the surrounding moisture. Convective precipitation (80% of annual precipitation over the domain), with generally larger and faster falling drops, is re-equilibrated to 45% versus 95% for stratiform precipitation. The bucket-type soil hydrology scheme does not account for surface and sub-surface drainage, groundwater formation, etc. Vapor fluxes from the surface are assumed to be dominantly transpiration by vegetation, and thus soil moisture is released into the atmosphere without fractionation [*Bariac et al.*, 1994b, 1994a].

[12] The present simulation by REMO$_{iso}$ was validated against data from the Global Network for Isotopes in Precipitation (GNIP) [*IAEA and WMO*, 2001] and ECHAM simulations by *Sturm et al.* [2007]. REMO was integrated over a period of 5 years, after one year spin-up. Lateral boundary conditions for winds, moisture, liquid water content and their isotopic counterparts were provided by an T42 ECHAM$_{iso}$ simulation at a 6 h time step. Sea-surface temperatures (SST) for both ECHAM and REMO are prescribed from the GISST climatology [*Rayner et al.*, 1994]. Mean monthly SST are linearly interpolated to provide 6 hour forcing to REMO. For any subsequent year, the models use the GISST climatology as a perpetual year. In conclusion, the boundary conditions are such that interannual variability, driven by SST, is removed. The simulation can be regarded as an ensemble run, focussing on the intraseasonal variability of the atmosphere.

### 2.2. Empirical Orthogonal Functions Analysis

[13] We apply an Empirical Orthogonal Function (EOF) analysis to selected variables in order to isolate their major intraseasonal variability. We discuss only the first EOF, which represents the dominant mode. It captures at least 20% of the variability for each selected variable. Simulated variables listed hereafter are analyzed for austral summer months (DJF) on a 5-day (pentad) resolution. We define hereafter EOF$_X$ (EC$_X$) and the spatial EOF pattern (temporal loadings) for parameter $X$.

[14] 1. Precipitation: 21% of the variance is captured in the first EOF.

[15] 2. Isotopic composition of precipitation ($\delta^{18}$O): 27% of the variance is captured in the first EOF.

[16] 3. Vertically integrated horizontal moisture transport $\mathbf{H} = H_u + H_v$ ($\mathbf{H} = \int_0^{TOA} Q(z) \cdot \mathbf{u}(z)\, \partial z$, where TOA stands for 'top of the atmosphere'. In this case, we applied the complex (or Hilbert) EOF method [*Venegas*, 2001] on $H^* = H_u + 1 \cdot H_v$, to account for the common variability of zonal and meridional moisture advection): 29% of the variance is captured in the first EOF. $H_u$ ($H_v$) represents the zonal (meridional) moisture advection.

[17] 4. Mean sea level pressure (SLP) (The leading EOFs of the sea-level pressure (SLP) and geopotential height at 200 hPa $\Phi_{200\text{hPa}}$ match in first order the topography. We suggest this first EOF to be an artefact of the computation technique: $SLP = P_s + \int_0^z - \frac{g}{R_d T_v(z)}\, \partial z$, where $g$: gravity acceleration, $R_d$: gas constant for dry air, $T_v(z)$: virtual subsurface temperature. In order to compute sea-level pressure at elevated grid points, we need to define a virtual atmospheric temperature profile below the surface. This virtual temperature was reconstructed on sub-surface pressure levels by a 3-D interpolation of surrounding atmospheric temperature. It is therefore biased by temperature variations along steep topography. The second EOF is not biased by altitude and is thus thought to represent the dominant mode of meteorological variability. The geopotential height is computed as a vertical integration of temperature-dependent air density, based on the SLP: $\Phi_{200\text{hPa}} = \int_{P=SLP}^{200\,\text{hPa}} \frac{-R_d T_v(P)}{g}\, \partial P$, with the same variable names as above.): 26% is captured in the meteorological dominant EOF.

[18] 5. Geopotential height at 200 hPa $\Phi_{200\text{hPa}}$: 20% is captured in the meteorological dominant EOF.

[19] Following *Dommenget and Latif* [2002] and *Björnsson and Venegas* [1997], we adopted several representations for EOF results. Figure 2 shows the EOF spatial patterns for precipitation (a), $\delta^{18}$O (b) and $H_v$ (c). This illustrates the dominant bi-modal variability in precipitation, with the positive poles in a crescent shape over the Atlantic off Belém, the Ecuadorian Amazon and the Paraná and the negative pole over the Nordeste and the neighboring Atlantic. The $\delta^{18}$O shows a similar pattern explained by the amount effect with high precipitation coinciding with low $\delta^{18}$O. As a result the $\delta^{18}$O EOF pattern has the opposite sign

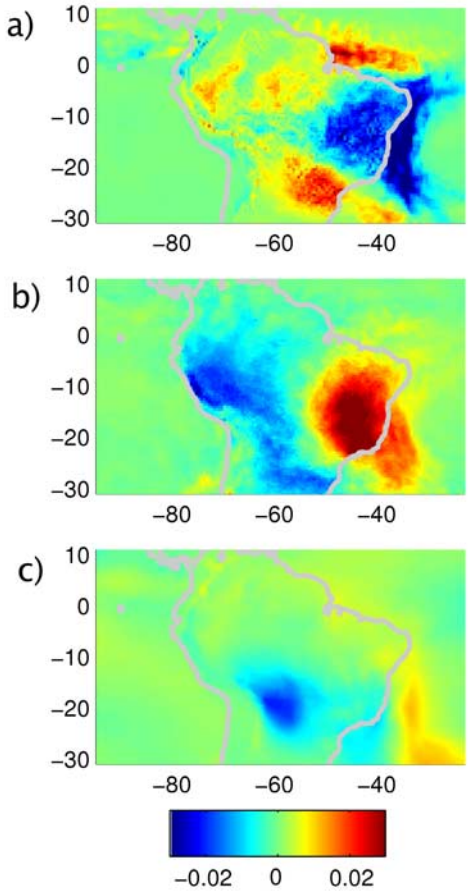


**Figure 2.** Leading empirical orthogonal function (EOF) pattern for summer (DJF) pentad (5-day) averaged variables. The first EOF is plotted for (a) precipitation, (b) isotopic composition of precipitation ($\delta^{18}$O), (c) meridional vapor transport ($H_v = \overline{Q \cdot \vec{v}} \cdot \vec{j}$, positive when flowing northward). All EOF are normalized, with red (blue) indicating positive (negative) EOF values. The color bar applies to all plots.

to $EOF_{Prec}$. The $\delta^{18}$O EOF shows a stronger relation between the Ecuadorian Amazon and the Paraná than for precipitation. The major feature of the $H_v$ EOF is a strong southward moisture transport centered over Santa Cruz [60°W; 20°S].

[20] Table 1 shows the correlation coefficients between the loadings (EC) of the variables cited above. $H_u$ and $H_v$ are independent and hence uncorrelated. Furthermore, $H_u$ is not or loosely correlated to all other variables, showing that the SAMS variability is instead captured by the $H_v$ variability. The cross-correlation of $\Phi_{200hPa}$ EC is generally lower than for *SLP*, demonstrating that the intraseasonal variability in our study is more related to low-level circulation than upper-level circulation. Finally, *Prec*, $\delta^{18}$O and $H_v$ are well correlated with each other ($R^2 > 41\%$). Figure 3 shows correlation maps between precipitation anomalies and the P (a), $\delta^{18}$O (b) and $H_v$ (c) loadings with all graphs displaying the same bi-modal pattern shown in Figure 2a. This indicates that a common phenomenon is responsible for the dominant variability mode. In the next section, we demonstrate this underlying phenomenon is related to SACZ/SAMS intraseasonal variability.

## 3. The Paraná - Nordeste Dipole

[21] Precipitation over the South American continent simulated by REMO displays a dipolar pattern, with one extremum over north-east Brazil at [40°W; 10°S] (hereafter referred to as Nordeste) and an opposite extremum over the south Brazil and Paraguay at [55°W; 25°S] (hereafter referred to as Paraná), as has been found in other studies [*Herdies et al.*, 2002; *Carvalho et al.*, 2002]. Alternation from one extreme to the other is mainly related to the location of the South Atlantic Convergence Zone (SACZ).

[22] In the present section, we first underline the dipolar pattern of precipitation as simulated with $REMO_{iso}$. We then investigate mechanisms in upper and lower level atmospheric motion related to this precipitation regime, to relate the bi-modal pattern to the comprehensive SAMS phenomenon. Finally, we analyze the isotopic signature of precipitation as an integrative proxy for precipitation and regional circulation patterns.

### 3.1. Oceanic Versus Continental SACZ Composites

[23] Figure 2a shows the first EOF of pentad austral summer (DJF) precipitation over South America characterized by the bi-modal pattern described above.

[24] On the basis of the first EOF of precipitation, we define the *oceanic SACZ composite* as the mean of pentads with loadings lower than the 25% percentile of $EC_{Prec}$. The 25% percentile is equal to −0.76 standard deviation of $EC_{Prec}$. Similarly, the *continental SACZ composite* merges all $EC_{Prec}$ pentads above the 75% percentile (+0.56 standard deviation). *Carvalho et al.* [2002, 2004] likewise associate precipitation regimes in sub-tropical America with the position of the SACZ: high precipitation over Paraná (Brazil east coast) occurs during dominantly continental (oceanic) location of the SACZ.

[25] The bimodal pattern in precipitation between the Nordeste and the Paraná is reported in several studies, based both on observations and simulations. However, authors use different criteria to define extreme phases of the dipole

**Table 1.** Correlation Coefficients *R* Between the Loadings (EC) Associated With the First EOF for Precipitation (Prec), Isotopic Composition of Precipitation ($\delta^{18}$O), Zonal ($H_u$) and Meridional ($H_v$) Vapor Transport, Mean Sea-Level Pressure (SLP) and Geopotential Height at 200 hPa ($\Phi$)[a]

| EC | Prec | $\delta^{18}$O | $H_u$ | $H_v$ | SLP | $\Phi_{200hPa}$ |
|---|---|---|---|---|---|---|
| **Prec** | 1 | 0.64 | 0.32 | 0.75 | 0.4 | 0.33 |
| **$\delta^{18}$O** | 0.64 | 1 | ⋆ | 0.76 | 0.53 | 0.3 |
| **$H_u$** | 0.32 | ⋆ | 1 | ⋆ | ⋆ | 0.26 |
| **$H_v$** | 0.75 | 0.76 | ⋆ | 1 | 0.57 | 0.22 |
| **SLP** | 0.40 | 0.53 | ⋆ | 0.57 | 1 | 0.45 |
| $\Phi_{200hPa}$ | 0.33 | 0.30 | 0.26 | 0.22 | 0.45 | 1 |
| $\overline{R^2}$ | 27% | 34% | | 38% | 24% | 10% |

[a]The mean common variance of one field with all the other is indicated in the last row ($\sigma^2$). ⋆ denotes correlations which fail the student-t significance test at the 90% level.

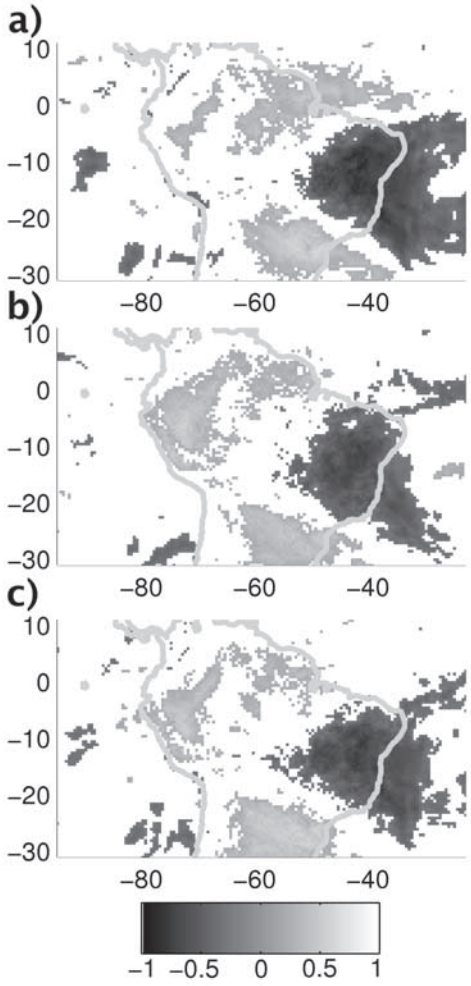


**Figure 3.** Correlation of precipitation over the whole study domain with the loadings (EC) associated to the first EOF for following parameters: (a) precipitation, (b) $\delta^{18}O$, (c) meridional moisture transport. Only correlations significant at 95% are displayed. Positive (negative) correlations are displayed in light (dark) grey. The color bar applies to all plots.

depending on the research focus. In the following paragraph, we briefly review climate parameters associated with extreme precipitation over the Paraná-Nordeste dipole.

[26] *Grimm et al.* [2004] use the first EOF of land precipitation to define intraseasonal modes. REMO reproduces similar results as *Grimm et al.* [2004] in both the dipole found in the first precipitation EOF as well as the seesaw shape of the second EOF (not shown). Using a slightly different approach, *Lenters and Cook* [1999] identify a similar dipole between the Paraná and Nordeste precipitation using EOF analysis of 5-day geopotential height at 200 and the Global Precipitation Index (GPI). A similar heterogeneous correlation map of the first loadings of the NASA-DAO geopotential height with global precipitation index (GPI) database further extends the negative correlation in Nordeste over the tropical Atlantic off the Brazil east coast. These observations are in agreement with similar correlation maps by $REMO_{iso}$ (not shown). *Doyle and Barros* [2002] investigate the interannual variability of summer precipitation over sub-tropical America, based on monthly NCEP reanalyses. Monthly precipitation displays a similar dipole between the Paraná and southern-eastern Brazil, which is found to be correlated to SST in western sub-tropical south Atlantic (WSSA). The continental (oceanic) composites by $REMO_{iso}$ correspond to the cold (warm) composites described by *Doyle and Barros* [2002].

### 3.2. Upper and Lower Level Atmospheric Motion

[27] *Geopotential height at* 200 hPa indicates the synoptic forcing of the SAMS. $EC_\Phi$ is poorly correlated to precipitation, with a squared correlation coefficient $r^2$ = 11% between their loadings. The dominant mode is consistent with the leading EOF from the NASA/DAO analyses *Lenters and Cook* [1999]. The strengthening of the Nordeste trough is associated with enhanced precipitation over the Paraná region.

[28] The vertical structure of the atmosphere under continental/oceanic SACZ conditions is shown in Figure 4. In the continental SACZ composite (Figure 4a), latent heat release by convection over central Amazon shifts the warm core anomaly to the West by ~5°. As a consequence, the Bolivian high follows the same shift, but its strength is not significantly altered. The oceanic composite (Figure 4b) moves the Bolivian high ~3° East of its climatological location, with high latent heat release related to enhanced convection off Brazil's East coast. In both cases, the Bolivian high does not undergo a clear latitudinal shift. Figure 4c shows the difference between the continental and oceanic SACZ composites, illustrating the eastward shift of the warm core at 400 hPa responsible for shifting the Bolivian high eastward at 200 hPa.

[29] Precipitation variability appears to be closely related to low-level circulation illustrated by the higher correlations between *SLP* and $H_v$ than for $\Phi_{200hPa}$. The relationship between $H_v$ variability and extreme events such as the LLJ warrants further discussion.

[30] $H_v$ reaches the next strongest correlation coefficient with precipitation $R^2$ = 56%. Its EOF (Figure 2c) is marked by an enhanced southwards flow above Santa Cruz [60°W; 20°S] associated with high precipitation over the Paraná, related to the frequency of LLJ events at this location [*Vera*, 2002]. Figure 4a shows that the core of the southwards wind during the continental SACZ composite is located at [50°W; 850 hPa]. Although $REMO_{iso}$ fails to represent the correct location of the mean southward winds (shifted eastward by 10°), it correctly captures that the variability at 60°W controls the Paraná precipitation (Figure 2c). The oceanic SACZ composite (Figure 4b) is marked by the absence of LLJ between 60°W and 50°W. Southwards winds are then predominant at 35°W, off Brazil's east coast. The difference between the continental and oceanic SACZ composites (Figure 4c) underlines the eastward shift of meridional winds between the continental and oceanic SACZ composites.

[31] These results are in good agreement with previous modeling studies. *Gan et al.* [2004] reports a similar opposition between LLJ paths in the oceanic/continental SACZ composites in the NCEP re-analyses. High precipitation in Western Central Brazil is associated with LLJ hedging an enhanced Chaco low, hence diverted from the Eastern flank of the Central Andes directly to the western

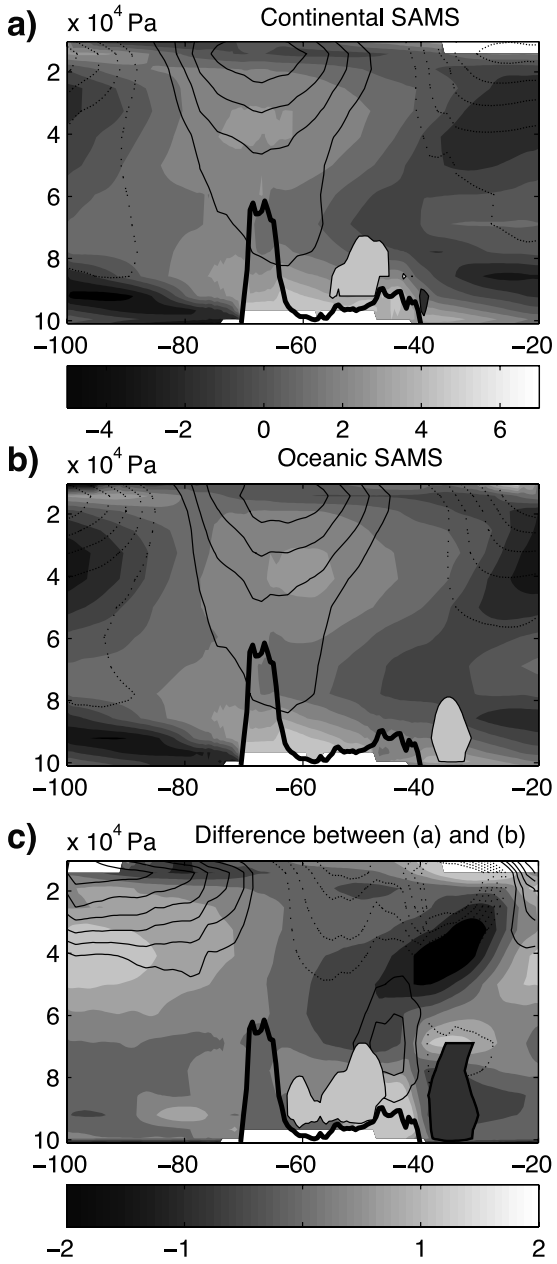


**Figure 4.** Vertical cross section along the 20°S parallel. Altitude is given in pressure levels (1e4 Pa). The thick black line represents the topography. (a) Continental SACZ composite, (b) oceanic SACZ composite, (c) difference between continental and oceanic SACZ. Colored shading represents the standing temperature eddy (difference from zonal mean, 1 K intervals for a–b, 0.5 K for (c), continuous (dashed) lines represent positive (negative) standing geopotential height eddies (20 m intervals for a–b, 5 m for c). The light (dark) grey filled contours represent southwards (northward) meridional winds ($\vec{v}$) above 6 m/s (a–b), or positive (negative) wind difference above 1 m/s (c).

flank of the Brazilian highlands. High precipitation over the Paraná is associated with a vanishing Chaco low, which enables LLJ to develop over Santa Cruz. Dominant LLJ at the western flank of the Brazilian highlands instead of the eastern flank of the Andes is simulated in both REMO and the RegCM2 RCM [*Rocha and Ambrizzi*, 2004]. *Vernekar et al.* [2003] on the other hand report a prevalence of Andean LLJ at 18°S. For further information, the reader is conferred to publications related to the SALLJEX experiment [*Vera*, 2002].

[32] Figure 5 shows a synthetic view of atmospheric dynamics associated with the SAMS. In the continental SACZ composite (Figure 5a), the Chaco low is located at [61°W; 22°S]. A strong South Atlantic high gives positive *SLP* anomaly over south-east Brazil [40°W; 20°]. This strong cyclonic flow implies a higher frequency of LLJ events, especially at [60°W; 18°S] (marked by arrows on 5a). This flow advects moist air from the Amazon basin with negative 'moist static stability' [*Lenters and Cook*, 1999], which favors convection over the Paraná region (as seen in the wind divergence at 200 hPa on Figure 5a). High precipitation over the Paraná is related to the continental location of the SACZ. The situation is reversed in the oceanic SACZ composite (Figure 5b). The Chaco low is strengthened and shifted north-eastward to [58°W; 18°S]. The south Atlantic high is weakened and shifted to the south-east. The reduced cyclonic flow redirects the warm moist Amazonian air to the Nordeste. The oceanic SACZ is then fed by maritime moisture, with strong convection (and upper-level divergence) off Brazil's east coast [35°W; 25°S]. Figure 5c illustrates the changes in *SLP* over south-east Brazil, and the related convection patterns.

[33] In conclusion, the analysis of lower and upper atmospheric circulation demonstrates that $REMO_{iso}$ accurately reproduces the mechanisms of the SAMS, as described by *Zhou and Lau* [1998] and *Vera et al.* [2006]. Intraseasonal variability of the SAMS can be represented by alternate continental and oceanic SACZ composites, which explains the bi-modal shape of precipitation (Figure 2a).

## 4. Stable Water Isotopes: An Integrated Proxy of the SAMS

[34] Given this validation of REMO to correctly simulate intraseasonal variability, we can extend our investigation to the water isotope diagnostics in $REMO_{iso}$: what does the $\delta^{18}O$ signature in precipitation reveal about the regional circulation patterns?

[35] The present study is innovative in its use of stable water isotopes to characterize the source and path of moisture from its isotopic signature. In this section, we concentrate on intraseasonal variability of $\delta^{18}O$ over South America, which has not been documented so far with isotope-enabled circulation models. Since summer precipitation represent 80% of the annual precipitation, and given the resolution of Andean ice cores over the last century, the intraseasonal variability will be recorded in isotopic archives and should strongly influence the mean annual $\delta^{18}O$ value.

### 4.1. $\delta^{18}O$ and Moisture Trajectory

[36] The climatological $\delta^{18}O$ pattern simulated by REMO is discussed by *Sturm et al.* [2007]: $REMO_{iso}$ is in reasonable agreement with GNIP observations and accurately reproduces the $\delta^{18}O$ pattern across tropical South America. Figure 6 shows the $\delta^{18}O$ for the continental (Figure 6a) and

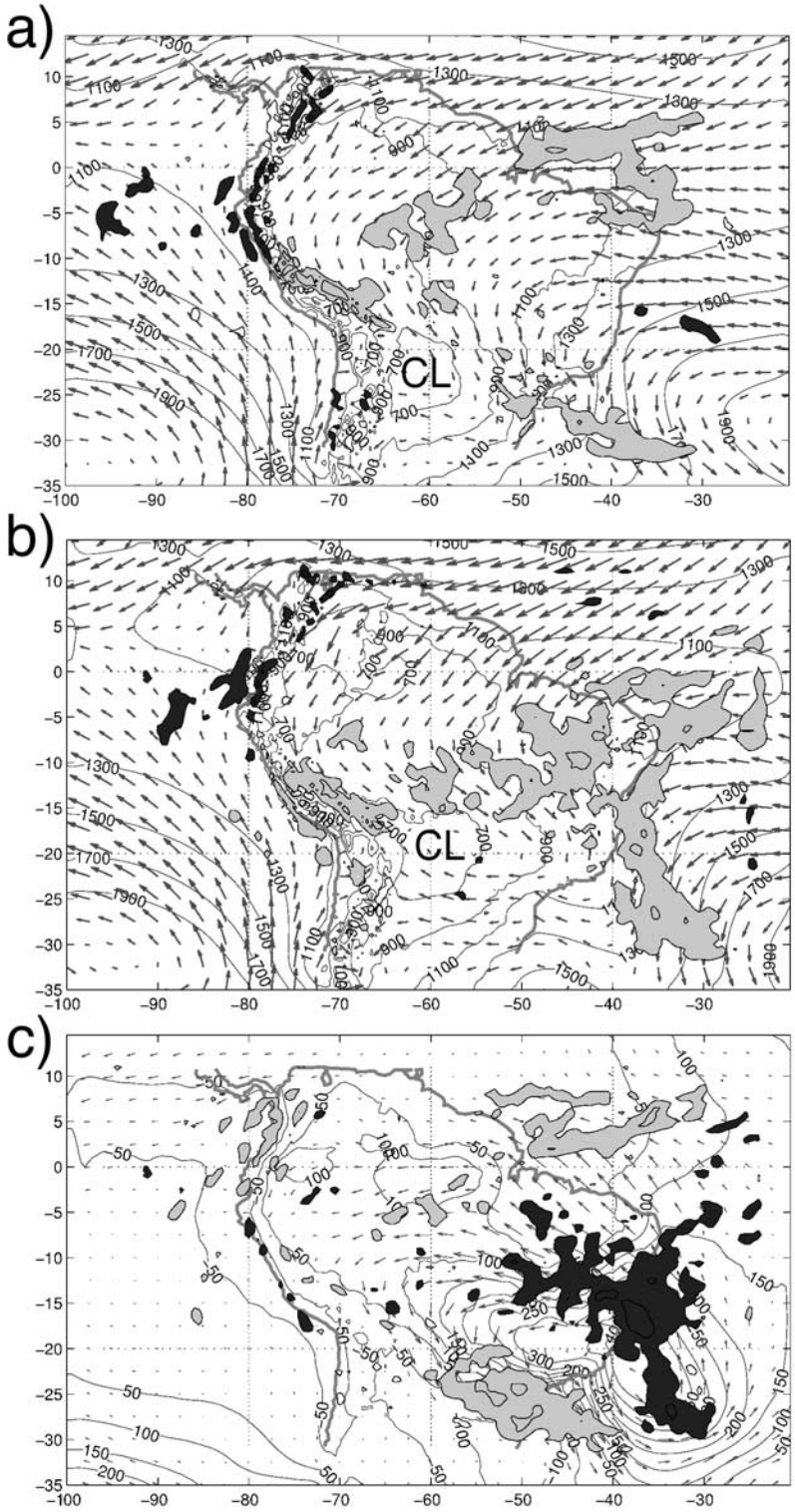


**Figure 5.** Atmospheric DJF circulation for the (a) the continental SACZ composite, (b) the oceanic SACZ composite, (c) the difference between the continental and oceanic SACZ composites. Mean sea level pressure is displayed in labeled contours, in hPa (with a 1e5 Pa subtracted from the mean). The light (dark) grey shaded areas represent wind divergence at 200 hPa above the 75% (below the 25%) percentile. Arrows represent the mean horizontal vapor advection $\vec{H}$. CL represents the location of the Chaco low.

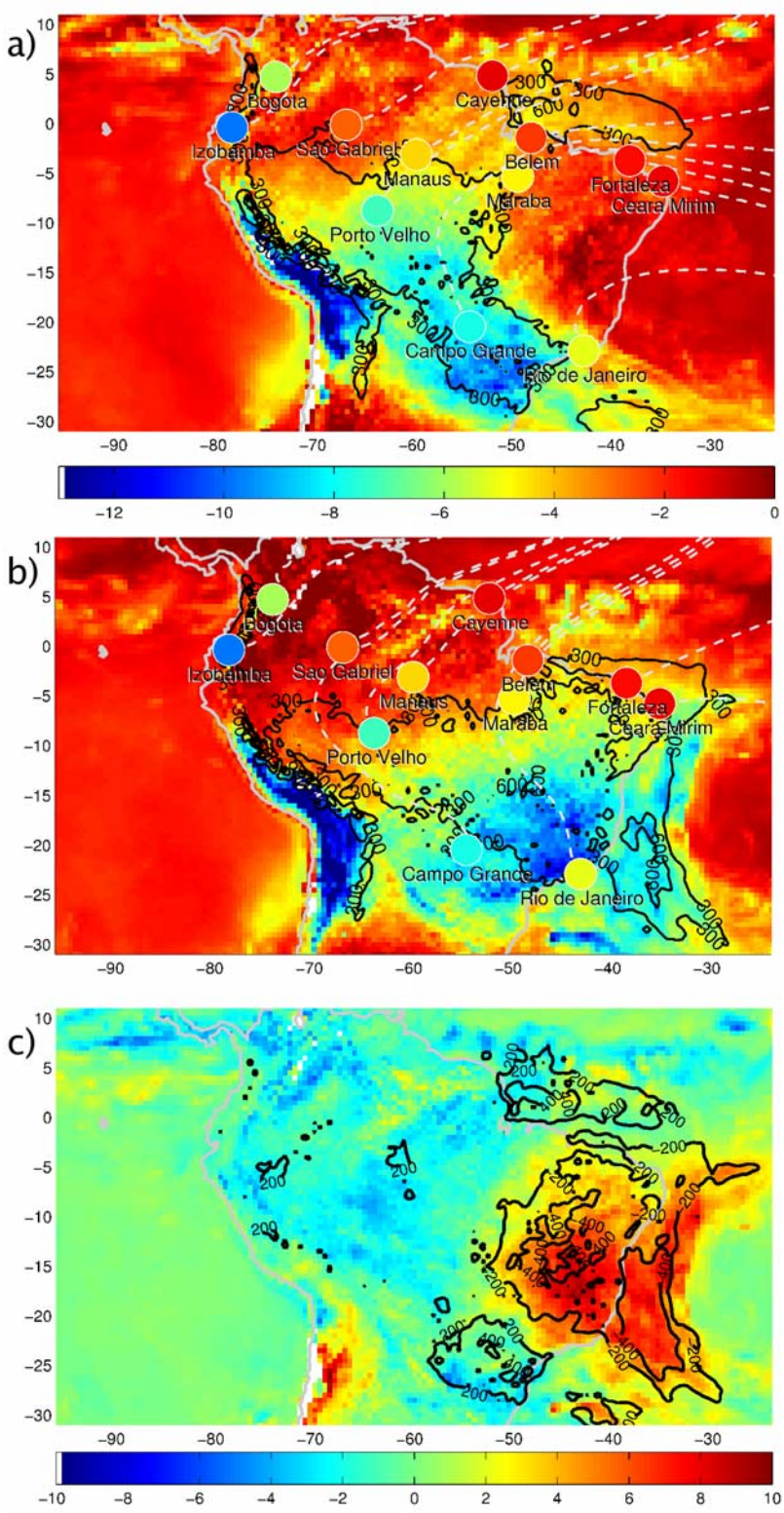


**Figure 6.** $\delta^{18}O$ in precipitation (shaded, in ‰) for the (a) the continental SACZ composite, (b) the oceanic SACZ composite, (c) the difference between the continental and oceanic SACZ composites. The top color bar (in ‰) applies to (a–b). The bottom color bar applies to the difference (c). The labeled contours represent total precipitation (with 300 mm/month interval). Colored dots represent $\delta^{18}O$ at GNIP stations, with their names displayed below. Since GNIP observations are available as monthly values only, the colors are identical for (a–b). The dotted grey lines represent streamlines (or back-trajectories) of mean horizontal moisture flux ($\mathbf{H} = \overline{Q \cdot \mathbf{u}}$).

the oceanic SACZ composites (Figure 6b). $\delta^{18}$O observations from the GNIP network are represented as colored dots. Trajectories (The mean wind directional constancy, calculated on the basis of 6 h wind speeds, is defined as $D_c = \frac{\|\overline{\vec{H}}\|}{\|\vec{H}\|} = \frac{\sqrt{\overline{H_u}^2 + \overline{H_v}^2}}{\sqrt{H_u^2 + H_v^2}}$. In case of steady winds, $D_c = 1$, and it decreases towards 0 if its direction is very variable. The wind constancy simulated by REMO$_{iso}$ in DJF is higher than 0.8 north of a line from [65°W; 15°S] to [44°W; 23°S]. This is consistent with previous studies [*Brahmananda Rao et al.*, 1996; *Garreaud*, 1999, 2000]. Hence, we can assume that streamlines are a valid estimation of the mean back-trajectories.) leading to the GNIP stations are also represented.

[37] On Figure 6, the $\delta^{18}$O pattern follows the precipitation iso-lines, illustrating the amount effect: heavy precipitation is characterized by low $\delta^{18}$O. According to the Rayleigh distillation theory, $\delta^{18}$O decreases exponentially with the cumulative precipitation along the trajectory. During the wet season, re-evaporation from the land-surface has a negligible effect on $\delta^{18}$O [*Sturm et al.*, 2007]. This illustrates the integrative character of the isotopic signal, with the $\delta^{18}$O of downstream precipitation retaining a memory of the rainout intensity along its trajectory.

[38] The integrative character $\delta^{18}$O of is responsible for strong connection between the Ecuadorian Amazon and the Paraná in the $\delta^{18}$O EOF pattern (Figure 2b). Strong precipitation over the Amazon is associated with strong precipitation over the Paraná, as demonstrated by the precipitation EOF (Figure 2a). The previous section on atmospheric circulation shows that air masses cross the Amazon before reaching the Paraná. Consequently the $\delta^{18}$O at the Paraná records both the increased local precipitation, as well as previous increased precipitation over the Amazon. Similarly, the correlation map of the $\delta^{18}$O EC with precipitation anomalies (Figure 3b) shows a stronger relationship between precipitation over the Amazon and the Paraná than for the precipitation EC (Figure 3a). This memory effect makes $\delta^{18}$O a better proxy for SAMS variability than precipitation alone.

[39] Table 1 shows that EC$_\delta$ shares an average 34% variance with all other loadings (second highest after EC$_{Hv}$). The highest correlation is reached for $\delta^{18}$O and meridional vapor transport $H_v$ ($R^2$ = 0.58%), whose EOF is maximum over Santa Cruz. This finding provides further support for the dominant role of LLJ in SAMS variability. Extreme precipitation related to LLJ have a typical duration of a few hours, with nighttime maxima [*Vernekar et al.*, 2003]. Pentad-averaged precipitation varies linearly with the occurrence of LLJ extreme precipitation events. Since $\delta^{18}$O decreases exponentially with precipitation amount, pentad-average $\delta^{18}$O is more likely to capture extreme precipitation events. This integrative characteristic becomes even more obvious at lower sampling frequencies. The typical SAMS dipole is recorded in the monthly $\delta^{18}$O anomalies, although they are not noticeable in monthly precipitation anomalies $\delta^{18}$O [*Sturm et al.*, 2007].

### 4.2. Regional Relevance of Station Measurements

[40] EOF analysis is a convenient method for analyzing physical processes responsible for spatial and temporal variability in gridded climate data sets. The previous subsection has shown that $\delta^{18}$O in particular is a good proxy of the SAMS variability, as simulated by REMO$_{iso}$. With no gridded data sets available for $\delta^{18}$O observations, we are required to base our analysis on station data. In this section we demonstrate that SAMS variability can be identified based on station records such as the rain-gage network over Bolivia [*Vimeux et al.*, 2005].

[41] To evaluate the use of station data to provide results coherent with the EOF method, five locations were selected for their representativeness of the SAMS variability, represented as boxes on Figure 1. In each 5 × 5° box, we compute the mean precipitation and weighted; these time series are hereafter referred to as 'box records', analogously to rain gauge and $\delta^{18}$O observations. These 'virtual' stations are centered at following locations:

[42] 1. The box including *Belém* is centered at [51.5°W; 3.5°S].

[43] 2. The *Ecuadorian Amazon* box is centered at [73.5°W; 4.5°S]. It lies on the eastern foothill of the Cordillera, at the origin of the Southern LLJ.

[44] 3. The *Nordeste* box is centered at [42.5°W; 9.5°S], at the Northern extension of the precipitation maximum in the oceanic SACZ composite.

[45] 4. The *Paraná* box is centered at [52.5°W; 28.5°S]. It marks the precipitation maximum in the continental SACZ composite.

[46] 5. The *Zongo* box is centered at [65.5°W; 14.5°S], at the foothills of the Altiplano. Extensive isotopic observations at daily and monthly time-scale have been conducted along this valley, as reported by *Vimeux et al.* [2005].

[47] Table 2 shows the cross-correlation coefficients between mean precipitation and $\delta^{18}$O for all five box records, including the loadings of precipitation and $\delta^{18}$O (EC$_{Prec}$ and EC$_\delta$). We first examine how box records individually correlate with SAMS variability, represented by EC$_{Prec}$ and EC$_\delta$. Then we investigate the cross-correlations between station records, to identify SAMS variability mechanisms without the help of EOFs.

[48] Precipitation from the Paraná and Nordeste boxes primarily illustrate the bi-modal pattern of the SAMS variability. In accordance with the EOF$_{Prec}$ pattern (Figure 2a), the correlation coefficient with EC$_{Prec}$ is strongly negative for Nordeste (R = −0.88) and positive for Paraná (R = 0.57). Significant positive correlations with EC$_{Prec}$ are also found all along the crescent-shaped continental SACZ maximum: Belém (R = 0.33), Ecuadorian Amazon (R = 0.34).

[49] $\delta^{18}$O is a better proxy for the SAMS variability than precipitation, because of its memory effect. As for precipitation, the $\delta^{18}$O in the Nordeste box is strongly anti-correlated with EC$_\delta$ (R = −0.76). Since the Ecuadorian Amazon and Zongo boxes are located in continental SACZ composite (2b), their $\delta^{18}$O is well correlated with EC$_\delta$ (Ecuadorian Amazon: R = 0.59, Zongo: R = 0.62).

[50] Table 2 (upper panel) summarizes the cross-correlations between box precipitation (corresponding to Figure 7). Sites typical for the continental SACZ composite (Ecuadorian Amazon and Paraná) are significantly correlated with each other (R = 0.3). Both are anti-correlated with the oceanic SACZ site (Nordeste, respectively R = −0.39 and R = −0.50). Back-trajectory computations show that the

**Table 2.** Correlation Coefficients Between Mean $\delta^{18}O$ and Precipitation Over Selected Locations[a]

| Stations | | Ec. Amazon | Nordeste | Paraná | Zongo | Belém | Prec | $\delta^{18}O$ |
|---|---|---|---|---|---|---|---|---|
| | | *Precipitation* | | | | | EC#1 | |
| Precipitation | **Ec. Amazon** | 1 | −0.39 | 0.30 | ⋆ | ⋆ | 0.34 | −0.62 |
| | **Ec. Amazon$^{-1}$** | 0.38 | −0.44 | 0.29 | ⋆ | ⋆ | 0.33 | −0.49 |
| | **Nordeste** | −0.39 | 1 | −0.50 | ⋆ | −0.27 | −0.88 | 0.70 |
| | **Paraná** | 0.30 | −0.5 | 1 | ⋆ | ⋆ | 0.57 | −0.55 |
| | **Zongo** | ⋆ | ⋆ | ⋆ | 1 | ⋆ | ⋆ | ⋆ |
| | **Belém** | ⋆ | −0.27 | ⋆ | ⋆ | 1 | 0.33 | ⋆ |
| | | $\delta^{18}O$ | | | | | EC#1 | |
| $\delta^{18}O$ | **Ec. Amazon** | 1 | −0.35 | ⋆ | 0.63 | ⋆ | −0.33 | 0.59 |
| | **Ec. Amazon$^{-1}$** | 0.5 | −0.43 | 0.22 | 0.3 | ⋆ | −0.39 | 0.57 |
| | **Nordeste** | −0.35 | 1 | −0.36 | −0.42 | 0.2 | 0.55 | −0.76 |
| | **Paraná** | ⋆ | −0.36 | 1 | ⋆ | ⋆ | −0.54 | 0.4 |
| | **Zongo** | 0.63 | −0.42 | ⋆ | 1 | −0.21 | −0.21 | 0.62 |
| | **Belém** | ⋆ | 0.20 | ⋆ | −0.21 | 1 | −0.38 | ⋆ |

[a]Each location is represented by a 5 × 5° box. The Ecuadorian Amazon box is centered at [73.5°W; 4.5°S], Nordeste at [42.5°W; 9.5°S], Paraná at [52.5°W; 28.5°S], Zongo at [65.5°W; 14.5°S], and Belém at [51.5°W; 3.5°S]. The Ecuadorian Amazon$^{-1}$, located to the west of the study domain, was correlated with a −1 pentad lag. The last two columns represent the loadings (EC) of the first EOF for precipitation and $\delta^{18}O$. ⋆ denotes correlations that fail the Student-t significance test at 90% level.

average traveltime for an air parcel from the Atlantic to the Zongo valley ranges from 6 [*Sturm et al.*, 2007] to 10 days [*Vimeux et al.*, 2005] during the wet season. Hence lagged (−1 pentad) correlations were computed for the Ecuadorian Amazon site, which increased the anti-correlation with the Nordeste (R = −0.44).

[51] Table 2 (lower panel) summarizes the cross-correlations for box $\delta^{18}O$. The correlation coefficients for $\delta^{18}O$ are generally larger than for precipitation. $\delta^{18}O$ appears therefore as a more consistent regional proxy of the SAMS variability. As for precipitation, the lagged correlation for the Ecuadorian Amazon results in more pronounced correlations with the Nordeste (R = −0.43) and the Paraná (R = 0.22). In the particular Zongo case, box $\delta^{18}O$ is strongly correlated with Ecuadorian Amazon $\delta^{18}O$ (R = 0.63) and significant anti-correlation with the Nordeste (R = −0.42). On the other hand, Zongo precipitation is not correlated to any other box precipitation records.

[52] The $\delta^{18}O$ precipitation box records were correlated with domain-wide precipitation, according to the methodology by *Dommenget and Latif* [2002]. We select four sites that record maximum SAMS variability, shown by 5 × 5° black boxes in Figure 7: Ecuadorian Amazon (Figure 7a), Nordeste (Figure 7b), Paraná (Figure 7c), and Zongo (Figure 7d). The correlation of the box with domain-wide precipitation is represented by shaded areas: light (dark) grey represent positive (negative) significant correlations. The significant correlations of box precipitation with domain-wide precipitation larger than 0.35 in absolute values is represented by contours: continuous grey (dashed black) lines represent positive (negative) lines.

[53] For all sites, the box precipitation is positively correlated with the surrounding precipitation (gray contin-

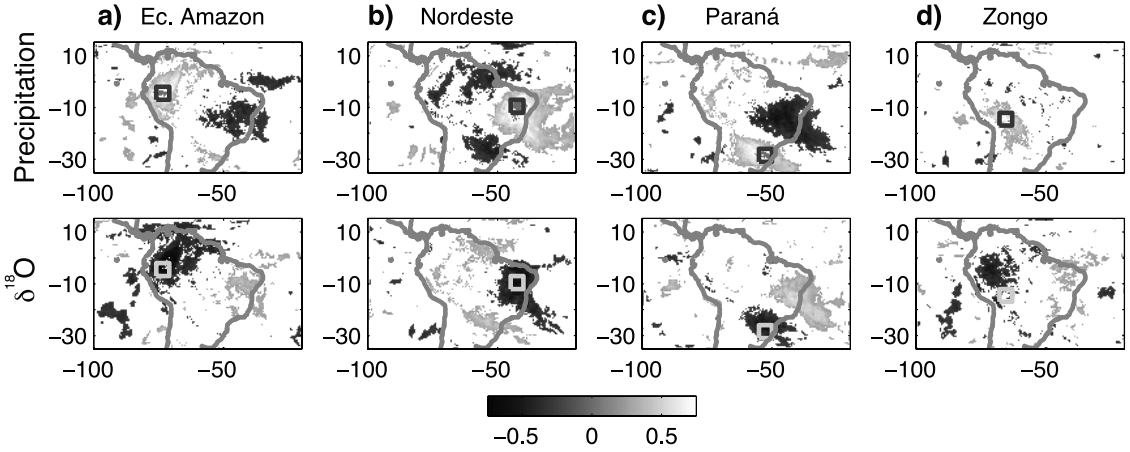


**Figure 7.** Correlation of box precipitation (upper row) and (lower row) with domain-wide precipitation. Only 95% significant correlations are plotted. The color bar is common to all sub-figures. The outlined boxes (identical to the boxes on Figure 1) represent the location of the sites: (a) the Ecuadorian Amazon (b) the Nordeste (c) Paraná, (d) Zongo valley at the foothills of the Altiplano. The exact box location in given in Table 2.

uous contours), showing the boxes are well representative of their area. In accordance with the precipitation EOF pattern (Figure 2a), the Ecuadorian Amazon and Paraná are anti-correlated with the Nordeste (black dashed contours on Figures 7a–7c). In contrast, precipitation in the Zongo box does not show any significant anti-correlation with poles of the oceanic SACZ composite.

[54] The correlation of box with domain-wide precipitation (shaded areas on Figure 7) illustrates the memory effect. Because of the amount effect, nearby upstream areas are negatively correlated with box: this is most obvious for the Ecuadorian Amazon (Figure 7a) and Zongo (Figure 7d) boxes. In both cases, the box correlations have a larger coverage than precipitation correlation: station is therefore a suitable proxy for regional summer precipitation. In accordance with the EOF pattern (Figure 2b), sites representative for the continental SACZ composite (Ecuadorian Amazon and Paraná) are anti-correlated with oceanic SACZ composite sites (Nordeste). The box correlation is particularly interesting in the Zongo case: although the local precipitation has only a local significance, the box shows a significant positive correlation with upstream regions typical for the continental SACZ composite (Ecuadorian Amazon), and negative correlation with the oceanic SACZ composite (Nordeste). This shows that from the Zongo box is a valid proxy for the intraseasonal SAMS variability, unlike the precipitation amount alone.

[55] In conclusion, correlations between station records and domain-wide precipitation reveals best the SAMS variability, in accordance with the EOF analysis. The superposition of correlation maps for the Ecuadorian Amazon, Zongo and Paraná stations (Figures 7a–7d) is an approximation of the EOF pattern (Figure 2b); the agreement is not perfect, because the sampling frequency (5 days) is in the same order of magnitude as the traveling time of vapor across the selected sites. This can be accounted for with lagged correlation (for the Ecuadorian Amazon site). The present modeling study offers a conceptual basis for further observation-based studies: box (and likewise station measurements) are likely to capture SAMS variability when correlated with gridded meteorological data sets.

## 5. Discussion

[56] The objective of the present section is to verify whether the SAMS mechanisms, as described in previous publications, are consistent with new evidence from the stable water isotopes. We first demonstrate that $REMO_{iso}$ represents the characteristic meteorological features of the South American Monsoon System. This is a pre-requisite for the analysis of the isotopic signal. Second, the variability confirms the dominant role of LLJ on the SACZ variability. Finally, we discuss the possible feedback between the atmosphere and the Atlantic sea-surface temperature controlling the SACZ.

[57] Interpretation of the isotopic signal is only justified if $REMO_{iso}$ accurately reproduces the SAMS variability. $REMO_{iso}$ accurately reproduces the mean summer climate across tropical South America [*Sturm et al.*, 2007], albeit excessive precipitation amounts. Hereafter, we discuss how REMO accounts for intraseasonal variability in comparison to both modeling and observational studies.

[58] The composite for maximum January precipitation over West-Central Brazil reported by *Gan et al.* [2004] exhibit the same circulation patterns as REMO oceanic SACZ composites. The Chaco low is enhanced and shifted to the North by 5°, together with a weakening of the South Atlantic high. Anomalous cyclonic circulation diverts the Amazonian airflow to the west instead of the south-west, where it converges with northerly Atlantic flow. Moist, unstable air convergence cause an intensification of the SACZ, which is shifted northward. Similar strengthening and northward shift of the SACZ is reported by *Carvalho et al.* [2002] and *Barreiro et al.* [2002]. It results in increased precipitation over Central-West Brazil, extending down to São Paolo. The atmospheric circulation simulated by $REMO_{iso}$ reproduces all these characteristics. Hence the intraseasonal variability simulated by $REMO_{iso}$ can be assimilated to SAMS variability.

[59] *Vernekar et al.* [2003] describes the simulation of South American summer climate at daily to inter-annual time-scales with the NCEP Eta RCM. LLJ develop with periodicity of 20 days. The role of LLJ is further documented by *Nogues-Paegle et al.* [2003], *Grimm et al.* [2004], and *Carvalho et al.* [2002].

[60] The present study reinforces the relevance of LLJ to the SAMS variability. The correlation of $EC_{Hv}$ in Table 1 is stronger with than with precipitation. Furthermore, since varies exponentially with precipitation amounts, low-resolution (up to monthly) records are a good proxy for extreme rain events related to LLJ. A fast Fourier transform (FFT) analysis on the $H_v$ loadings reveal two minor peaks at 13 and 14 day periods, with larger peaks at 24 and 51 day period. Hence REMO seems to capture correctly the $\sim$20 day cyclicity of LLJ. According to *Paegle et al.* [2000] and *Carvalho et al.* [2004], the $\sim$ 50-day periodicity could represent the modulation of SACZ activity by the Madden-Julian Oscillation (MJO) over the tropical Pacific.

[61] *Doyle and Barros* [2002] present an extensive study on inter-annual Atlantic SST anomalies and related circulation patterns over Subtropical South America. Monthly SST in the western sub-tropical South Atlantic (WSSA) is found to be correlated with the position and intensity of the SACZ, hence with precipitation patterns over sub-tropical South America. *Barreiro et al.* [2002] identify similar correlations between precipitation EOF loadings and South Atlantic SST indices in ensemble runs with the CCM3 GCM: SST forcing explains a significant part of the SACZ variability over the Atlantic, but has little influence on the variability of continental precipitation. The C (W) composite defined by *Doyle and Barros* [2002] corresponds to the oceanic (continental) SACZ composite simulated by $REMO_{iso}$, although $REMO_{iso}$ is driven by climatological SSTs.

[62] The contradiction can be resolved by considering the SACZ variability as being primarily of atmospheric origin, with positive feedback from the surface ocean. Singular value decomposition show that sea level pressure lead SST changes by 1–2 months [*Venegas et al.*, 1997], indicating an atmosphere-to-ocean forcing. The SACZ location in its continental composite tends to decrease the SST over the WSSA. The enhanced cloudiness reduces the radiative heating of surface ocean, and increased surface winds mix the ocean boundary layer. The negative SST anomalies in turn enhance the temperature contrast between land and

ocean, strengthening a giant land-sea breeze that intensifies the oceanic SACZ. Furthermore, the Brazilian Current flowing along the east Brazil coast advects negative SST anomalies to the South. Similar to *Lenters and Cook*'s [1999] second mechanism, the cold-core subtropical low is strengthened, thus enhancing moist westward flow into the oceanic SACZ and helping maintaining a strong SACZ activity on seasonal time-scales.

[63] In conclusion, the short integration (5 years) of REMO using climatological SSTs primarily reflects the intraseasonal, atmospheric variability of the SACZ. The variability is highest over land, where feedbacks by energy and moisture exchanges with the surface strengthen the stochastic behavior of the SAMS. Nevertheless, the fact that the variability patterns agree well with observations and coupled model studies suggest an atmosphere-to-ocean forcing between the SACZ and South Atlantic SST. The lack of a coupled ocean model in REMO merely limits the positive feedback from SST on the SACZ, which could affect the persistence of the simulated SACZ.

## 6. Summary and Conclusion

[64] The present study investigates the intraseasonal variability of austral summer (DJF) South American climate based on a 5-year integration of the regional circulation model $REMO_{iso}$ with climatological SST. We choose a 5-day (pentad) sampling frequency and perform an EOF analysis on different climate parameters: precipitation, 200 hPa geopotential height, mean sea level pressure and vertically integrated moisture transport. The goal of the present study is to investigate the stable water isotope signal in precipitation and relate it to the bimodal precipitation pattern and related SAMS mechanisms.

[65] Intraseasonal variability during austral summer is marked by a bimodal shape, with contrasting poles over the Paraná [55°W; 25°S] and the Nordeste [40°W; 10°S]. The EOF pattern of pentad precipitation (Figure 2a) illustrates this pattern. It further reveals a weaker connection between high precipitation over the Paraná and the Amazon, forming a crescent-shaped counterpart to low precipitation over Eastern Brazil (Nordeste). This dipole structure is widely documented in both observation and modeling studies [*Vera et al.*, 2006; *Herdies et al.*, 2002; *Grimm et al.*, 2004; *Lenters and Cook*, 1999; *Doyle and Barros*, 2002; *Carvalho et al.*, 2002, 2004; *Barreiro et al.*, 2002; *Lau and Zhou*, 2003; *Barros et al.*, 2003; *Gan et al.*, 2004; *Nogues-Paegle et al.*, 2003].

[66] The simulated precipitation variability is physically related to alternating atmospheric circulation patterns. In the case of a predominantly continental location of the South Atlantic convergence zone (SACZ) (Figure 5), the Chaco low shifts southwards and South Atlantic high is strengthened. The cyclonic flow in turn is enhanced, which increases meridional advection of moist Amazonian air to the Paraná by means of more frequent low-level jets (LLJ) above Santa Cruz [60°W; 20°S]. In the opposite case (oceanic SACZ composite - Figure 5b), Amazonian moisture is diverted zonally toward east Brazil. This leads to a north-eastern shift of the SACZ. The interaction between the SACZ location, changes of regional circulation patterns and resulting precipitation variability are summarized in the South American monsoon system (SAMS).

[67] This variability in precipitation intensity and trajectory is distinctively recorded in the stable water isotope signal. The amount effect accounts for anti-correlation between $\delta^{18}O$ and precipitation. Furthermore, $\delta^{18}O$ decreases exponentially with the cumulative rain-fall along its trajectory. Hence $\delta^{18}O$ is a better proxy for the SAMS variability than precipitation alone, since its 'memory effect' enhances the impact of LLJ on bi-modal $\delta^{18}O$ EOF pattern. In particular, $\delta^{18}O$ at the Zongo location [65.5°W; 14.5°S] proves to be a sensitive proxy for the SAMS variability. This result has wide-ranging implications for the interpretation of, e.g., the Illimani ice core, located uphill the Zongo valley. Since 80% of the precipitation occurs in summer, the annual $\delta^{18}O$ will be strongly influenced by summer circulation variability. Could the $\delta^{18}O$ record measured in the Illimani ice core be used to reconstruct the predominance of oceanic versus continental SACZ in the past? This question can only be answered by separating the competing controls on precipitation $\delta^{18}O$ across South America. The present study indicates that internal, atmospheric variability has the potential to strongly influence the $\delta^{18}O$ signal in the Illimani ice core and Brazilian speleothems.

[68] In conclusion, the present study introduces a high resolution simulation of the stable water isotopes in precipitation over South America. It underlines the benefits of improved topography in representing mesoscale features, such as the low-level jets, and their influence $\delta^{18}O$ on variability at intraseasonal timescale. Nevertheless, longer integrations of $REMO_{iso}$ with observed sea-surface temperatures are needed to determine the mechanisms on interannual time-scales. Using the same analysis methods as described in the present study, the isotopic signal can be used to identify how internal, intraseasonal variability (e.g., SAMS) is modulated by external, SST-driven forcing (e.g., ENSO in the Pacific, or Atlantic WSSA variability).

[69] **Acknowledgments.** The authors would like to thank Matthias Vuille, Martin Werner and the anonymous reviewers for their valuable comments. We thank S.J. Birks for proofreading the manuscript. Simulations were performed at the German High Performance Computing Centre for Climate- and Earth System Research (DKRZ, Hamburg). The present study was supported by French Science Foundation grant ACI 'Changement climatique et cryopshère' and the Amancay (INSU/LEFE) grant.

## References

Bariac, T., J. Gonzalez-Dunia, N. Katerji, O. Béthenod, J. Bertolini, and D. Mariotti (1994a), Spatial variation of the isotopic composition of water ($^{18}O$, $^{2}H$) in organs of aerophytic plants: 2. Assessment under field conditions, *Chem. Geol.*, *115*(3–4), 317–333.

Bariac, T., J. Gonzalez-Dunia, F. Tardieu, T. Tessier, and D. Mariotti (1994b), Spatial variation of the isotopic composition of water ($^{18}O$, $^{2}H$) in organs of aerophytic plants: 1. Assessment under laboratory conditions, *Chem. Geol.*, *115*(3–4), 307–315.

Barreiro, M., P. Chang, and R. Saravanan (2002), Variability of the south Atlantic convergence zone simulated by an atmospheric general circulation model, *J. Clim.*, *15*, 745–763.

Barros, V., M. Doyle, M. González, I. Camilloni, R. Bejarán, and R. Caffera (2003), Climate variability over subtropical South America and the South American monsoon: A review, *Meteorologica*, *27*(1–2), 33–57.

Björnsson, H., and S. Venegas (1997), A manual for EOF and SVD Analyses of Climate Data, *Tech. rep.*, Center for Climate and Global Change Research, McGill Univ., http://www.dcess.ku.dk/silvia/eofsvd/eofsvd.html.

Bradley, R. S., M. Vuille, D. Hardy, and L. G. Thompson (2003), Low latitude ice cores record Pacific sea surface temperatures, *Geophys. Res. Lett.*, *30*(4), 1174, doi:10.1029/2002GL016546.

Brahmananda Rao, V., I. F. A. Cavalcanti, and K. Hada (1996), Annual variation of rainfall over Brazil and water vapor characteristics over South America, *J. Geophys. Res.*, *101*(10), 26,539–26,552.

Carvalho, L. M. V., C. Jones, and B. Liebmann (2002), Extreme precipitation events in southeastern South America and large-scale convective patterns in the South Atlantic convergence zone, *J. Clim.*, *15*, 2377–2394.

Carvalho, L. M. V., C. Jones, and B. Liebmann (2004), The South Atlantic convergence zone: Intensity, form, persistence, and relationships with intraseasonal to interannual activity and extreme rainfall, *J. Clim.*, *17*, 88–108.

Chiang, J. C. H., and A. H. Sobel (2002), Tropical Tropospheric Temperature Variations Caused by ENSO and Their Influence on the Remote Tropical Climate, *J. Climate*, *15*, 2616–2631, doi:10.1175/1520-0442(2002)015<2616:TTTVCB>2.0.CO;2.

Chou, S. C., A. M. B. Nunes, and I. F. A. Cavalcanti (2000), Extended range forecasts over South America using the regional eta model, *J. Geophys. Res.*, *105*(8), 10,147–10,160.

Cruz, F. W., S. J. Burns, I. Karmann, W. D. Sharp, and M. Vuille (2006), Reconstruction of regional atmospheric circulation features during the late Pleistocene in subtropical Brazil from oxygen isotope composition of speleothems, *Earth Planet. Sci. Lett.*, *248*, 495–507, doi:10.1016/j.epsl.2006.06.019.

Dommenget, D., and M. Latif (2002), A Cautionary Note on the Interpretation of EOFs., *J. Clim.*, *15*, 216–225.

Doyle, M. E., and V. R. Barros (2002), Midsummer low-level circulation and precipitation in subtropical South America and related sea surface temperature anomalies in the south Atlantic, *J. Clim.*, *15*, 3394–3410.

Gan, M., V. Kousky, and C. Ropelewski (2004), The South American monsoon circulation and its relationship to rainfall over west-central Brazil, *J. Clim.*, 47–66.

Garreaud, R. (1999), Cold air incursions over subtropical and tropical South America. A numerical case study, *Mon. Weather Rev.*, *127*, 2823–2853.

Garreaud, R. (2000), Cold air incursions over Subtropical South America: Mean structure and dynamics, *Mon. Weather Rev.*, *128*, 2544–2559.

Grimm, A., C. Vera, and C. Mechoso (2004), The South American Monsoon System, in *Third International Workshop on Monsoons (IWM-III)*, edited by C. Chang, pp. 23–41, World Meteorological Organisation, Hangzhou, China, http://www.nps.edu/Academics/gseas/IWM-III/Index.html.

Henderson, K. A., L. G. Thompson, and P.-N. Lin (1999), Recording of El Niño in ice core $\delta^{18}$O records from Nevado Huascarán, Peru, *J. Geophys. Res.*, *104*(13), 31,053–31,066.

Herdies, D. L., A. da Silva, M. A. F. Silva Dias, and R. Nieto Ferreira (2002), Moisture budget of the bimodal pattern of the summer circulation over South America, *J. Geophys. Res.*, *107*(D20), 8075, doi:10.1029/2001JD000997.

Hoffmann, G. (2003), Taking the pulse of the tropical water cycle, *Science*, *301*, 776–777.

Hoffmann, G., M. Werner, and M. Heimann (1998), Water isotope module of the ECHAM atmospheric general circulation model: A study on timescales from days to several years, *J. Geophys. Res.*, *103*(14), 16,871–16,896.

Hoffmann, G., et al. (2003), Coherent isotope history of Andean ice cores over the last century, *Geophys. Res. Lett.*, *30*(4), 1179, doi:10.1029/2002GL014870.

I. A. E. A., and W. M. O. (2001), The Global Network of Isotopes in Precipitation (GNIP) database, ''http://isohis.iaea.org''.

Jacob, D., et al. (2001), Comprehensive model intercomparison study investigating the water budget during the BALTEX-PIDCAP period, *Meteorol. Atmos. Phys.*, *77*, 19–43.

Jouzel, J., and L. Merlivat (1984), Deuterium and oxygen 18 in precipitation: Modeling of the isotopic effects during snow formation, *J. Geophys. Res.*, *89*, 11,749–11,757.

Lau, K., and J. Zhou (2003), Anomalies of the South American summer monsoon associated with the 1997–99 El Niño-Southern Oscillation, *Int. J. Climatol.*, *23*, 529–539.

Lenters, J. D., and K. Cook (1999), Summertime precipitation variability in South America: Role of the large-scale circulation, *Mon. Weather Rev.*, *127*(3), 409–443.

Majewski, D. (1991), The Europa-Model of the Deutscher Wetterdienst, *ECMWF Seminar on numerical methods in atmospheric models*, *2*, 147–191.

Majoube, M. (1971), Fractionnement en oxygène 18 et en deutérium entre l'eau et sa vapeur, *J. Chem. Phys.*, *10*, 1423–1436.

Merlivat, L., and J. Jouzel (1979), Global climatic interpretation of the deuterium-oxygen 18 relationship for precipitation, *J. Geophys. Res.*, *84*, 5029–5033.

Nogues-Paegle, J., et al. (2003), Progress in Pan American CLIVAR research: Understanding the South American monsoon, *Meteorologica*, *27*(1–2), 1–30.

Paegle, J., L. A. Byerle, and K. C. Mo (2000), Intraseasonal modulation of south American summer precipitation, *Mon. Weather Rev.*, *128*(3), 837–850.

Pierrehumbert, R. T. (1999), Huascaran $\delta^{18}$O as an indicator of tropical climate during the Last Glacial Maximum, *Geophys. Res. Lett.*, *26*, 1345–1348.

Ramirez, E., et al. (2003), A new Andean deep ice core from Nevado Illimani (6350 m), Bolivia, *Earth Planet. Sci. Lett.*, *212*, 337–350.

Rayner, N., D. Parker, E. Horton, C. Folland, and R. Hackett (1994), Version 2.2 of the Global Sea-Ice and Sea Surface Temperature Data Set, 1903– 1994, *Climate Research Technical Note 74*, Hadley Centre, http://www.metoffice.com/research/hadleycentre/obsdata/GISST.html.

Rocha, R., and T. Ambrizzi (2004), Regional Climate Model2 simulations of the Low Level Jet East of the Andes, in *CLIVAR Science Conference*, Baltimore, http://www.clivar2004.org/electronic%20posters/monsoon_table.html.

Roeckner, E., et al. (1996), The atmospheric circulation model ECHAM-4: model description and simulation of the present day climate, *Max-Planck-Institute für Meteorologie Report*, *218*.

Rojas, M., and A. Seth (2003), Simulation and sensitivity in a nested modeling system for South America. Part II: GCM boundary forcing, *J. Clim.*, *16*, 2454–2471.

Seth, A., and M. Rojas (2003), Simulation and sensitivity in a nested modeling system for South America. Part I: Reanalyses boundary forcing, *J. Clim.*, *16*, 2437–2453.

Seth, A., M. Rojas, B. Liebmann, and J.-H. Qian (2004), Daily rainfall analysis for South America from a regional climate model and station observations, *Geophys. Res. Lett.*, *31*, L07213, doi:10.1029/2003GL019220.

Sturm, K., G. Hoffmann, B. Langmann, and W. Stichler (2005), Simulation of $\delta^{18}$O in precipitation by the regional circulation model REMO$_{iso}$, *Hydrol. Processes*, *19*, 3425–3444, doi:10.1002/hyp.5979.

Sturm, C., G. Hoffmann, and B. Langmann (2007), Climatology of stable water isotopes in South America: Comparing general to regional circulation models, *J. Clim.*, in press, doi:10.1175/JCLI4194.1.

Thompson, L. G. (2000), Ice core evidence for climate change in the Tropics: implications for our future, *Quat. Sci. Rev.*, *19*(1–5), 19–35, doi:10.1016/S0277-3791(99)00052-9.

Thompson, L. G., E. Mosley-Thompson, M. E. Davis, P.-N. Lin, K. A. Henderson, J. Cole-Dai, J. F. Bolzan, and K.-B. Liu (1995), Late Glacial Stage and Holocene Tropical Ice Core Records from Huascaran, Peru, *Science*, *269*:46–50, July .

Thompson, L. G., et al. (1998), A 25000-Year Tropical Climate History from Bolivian Ice Cores, *Science*, *282*, 1858.

Thompson, L. G., E. Mosley-Thompson, and K. A. Henderson (2000), Ice-core palaeoclimate records in tropical South America since the Last Glacial Maximum, *J. Quarter. Sci.*, *15*, 377–394.

Venegas, S. (2001), Statistical Methods for Signal Detection in Climate, *Tech. rep.*, Danish Center for Earth System Science, http://www.dcess.ku.dk/silvia/.

Venegas, S. A., L. A. Mysak, and D. N. Straub (1997), Atmosphere-ocean coupled variability in the South Atlantic, *J. Clim.*, *10*, 2904–2920.

Vera, C. (2002), Introduction to the SALLJ conference and SALLJEX field campaign, in *VAMOS/CLIVAR/WCRP Conference on South-American low-level jets*, Santa Cruz de la Sierra, Bolivia, http://www.salljex.at.fcen.uba.ar/sallj/.

Vera, C., et al. (2006), Toward a unified view of the American monsoon systems, *J. Clim.*, *19*(20), 4977–5000, doi:10.1175%2FJCLI3896.1.

Vernekar, A. D., B. P. Kirtman, and M. J. Fennessy (2003), Low-level jets and their effects on the South American summer climate as simulated by the NCEP Eta model, *J. Clim.*, *16*, 297–311.

Vimeux, F., R. Gallaire, S. Bony, G. Hoffmann, and J. Chiang (2005), What are the controls on (D in precipitation in the Zongo Valley (Bolivia)? Implications for the Illimani ice core interpretation, *Earth and Planetary Science Lett.*, doi:10.1016/j.epsl.2005.09.031.

Vuille, M., and M. Werner (2005), Stable isotopes in precipitation recording South American summer monsoon and ENSO variability - Observations and model results, *Clim. Dyn.*, *25*(4), 401–413, doi:10.1007/s00382-005-0049-9.

Vuille, M., R. S. Bradley, R. Healy, M. Werner, D. R. Hardy, L. G. Thompson, and F. Keimig (2003a), Modeling $\delta^{18}$O in precipitation over the tropical Americas: 2. Simulation of the stable isotope signal in Andean ice cores, *J. Geophys. Res.*, *108*(D6), 4175, doi:10.1029/2001JD002039.

Vuille, M., R. S. Bradley, M. Werner, R. Healy, and F. Keimig (2003b), Modeling $\delta^{18}O$ in precipitation over the tropical Americas: 1. Interannual variability and climatic controls, *J. Geophys. Res.*, *108*(D6), 4174, doi:10.1029/2001JD002038.

Wang, X., A. S. Auler, R. L. Edwards, H. Cheng, P. S. Cristalli, P. L. Smart, D. A. Richards, and C.-C. Shen (2004), Wet periods in northeastern Brazil over the past 210kyr linked to distant climate anomalies, *Nature*, *432*, 740–743, doi:10.1038/nature03067.

Werner, M., and M. Heimann (2002), Modeling interannual variability of water isotopes in Greenland and Antarctica, *J. Geophys. Res. (Atmospheres)*, *107*(1), 1.

Zhou, J., and K.-M. Lau (1998), Does a monsoon climate exist over South America?, *J. Clim.*, *11*, 1020–1040.

G. Krinner and C. Sturm, Laboratoire de Glaciologie et Géophysique de l'Environnement, BP 96, 38402 Saint-Martin-d'Hères Cedex, France. (kristof.sturm@bjerknes.uib.no)

F. Vimeux, IRD-UR Great Ice, IPSL/LSCE (Laboratoire des Sciences du Climat et de l'Environnement), Gif-sur-Yvette, France.